



Microporous core-shell $\text{Co}_{11}(\text{HPO}_3)_8(\text{OH})_6/\text{Co}_{11}(\text{PO}_3)_8\text{O}_6$ nanowires for highly efficient electrocatalytic oxygen evolution reaction

Yueran Ni^{a,b,1}, Bowen He^{c,1}, Siyuan Luo^b, Xiaoyong Wu^a, Xuezheng Feng^b, Yi Luo^d, Jia Lin^e, Junliang Sun^f, Ke Fan^{c,*}, Yongfei Ji^{g,*}, Gaoke Zhang^{a,*}, Hong Chen^{b,*,2}

^a Hubei Key Laboratory of Mineral Resources Processing and Environment, School of Resources and Environmental Engineering, Wuhan University of Technology, Wuhan 430070, China

^b School of Environmental Science and Engineering, Guangdong Provincial Key Laboratory of Soil and Groundwater Pollution Control, Key Laboratory of Municipal Solid Waste Recycling Technology and Management of Shenzhen City, Southern University of Science and Technology, Shenzhen 518055, China

^c State Key Laboratory of Advanced Technology for Materials Synthesis and Processing, Wuhan University of Technology, Wuhan 430070, China

^d Department of Materials and Environmental Chemistry Stockholm University, SE-106 91 Stockholm, Sweden

^e Department of Physics, Shanghai University of Electric Power, Shanghai 200090, China

^f College of Chemistry and Molecular Engineering, Peking University, Beijing 100871, China

^g School of Chemistry and Chemical Engineering, Guangzhou University, Guangzhou 510006, China

ARTICLE INFO

Keywords:

Oxygen evolution reaction
Nanowires
Heterostructure
Core-shell
Cobalt phosphite

ABSTRACT

Exploring high-efficient oxygen evolution reaction (OER) catalysts is critical for producing clean H_2 fuel through water splitting. Co and P involved Co-Pi and cobalt phosphide OER catalysts attracted tremendous attention, while limited report on cobalt phosphite as an OER catalyst. Herein, a novel cobalt phosphite nanowires with microporous 1D channel have been successfully discovered with remarkable catalytic performance of a low overpotential of ~ 340 mV and Tafel slope of 60 mV dec^{-1} at 10 mA cm^{-2} at pH 14. Through comprehensive structural characterization, the effective species has been clearly illustrated to be the *in-situ* formed heterostructural $\text{Co}_{11}(\text{HPO}_3)_8(\text{OH})_6/\text{Co}_{11}(\text{PO}_3)_8\text{O}_6$ core-shell structure nanowires. This work fills the gap for exploring high efficient cobalt phosphites OER catalysts under alkaline condition and paves the way for exploring novel high efficiency water splitting catalysts.

1. Introduction

With the increasing energy demanding and the crisis of environmental pollution, the searching of efficient catalysts development for renewable energy has been attracting more and more attention [1–5]. Water splitting regarding as one of the environmental-friendly strategies for energy production and industry ecology development has arisen a lot of attention [6–8]. Due to the thermodynamic convenience and practical application in alkaline electrolysis cells, great efforts have been devoted to developing oxygen evolution reaction (OER) catalysts at strong alkaline conditions [9–11]. Among the highly efficient catalysts, noble-metal-based electrocatalysts, such as IrO_2 and RuO_2 , have been the benchmark toward OER, while they suffer from the scarcity and high cost of these noble metals [12–14]. Therefore, new effort has been devoted to the development of catalysts based on earth-abundant elements [15–17]. Among them, Co-Pi catalysts based on $\text{Co}^{2+}\text{-PO}_4^{3-}$

firstly discovered by Nocera et al. [18] with low catalytic overpotential and high current density has emerged as promising non-noble metal water-splitting catalysts. The first Co-Pi catalyst reported by Nocera is a highly porous structure *in-situ* formed from the $\text{Co}^{2+}\text{-PO}_4^{3-}$ rich electrolyte. The catalyst exhibited good catalytic performance at neutral pH. After the discovering of the Co-Pi catalyst, tremendous photochemical or photoelectrochemical devices have been fabricated by employing the Co-Pi catalyst in the anode part for OER. Later, other $\text{Co}^{2+}\text{-PO}_4^{3-}$ based catalysts, such as $\text{H}_2\text{-CoCat}$ [19], $\text{Co}_3(\text{PO}_4)_2\text{-N-C}$ [20] have been also explored. Although the Co-phosphate OER catalyst family grow fast in a short time, the reported catalytic efficiency of the catalysts has been developing in relatively slow steps. Later, tremendous effort has been devoted into other type of $\text{Co}^{2+}\text{-P}^{3-}$ combination of catalyst, which is the cobalt phosphide (Co_xP) catalysts. Benefitting from the great electron transfer property and good stability, Co_xP family catalysts stand out as a rising star for OER reaction

* Corresponding authors.

E-mail addresses: kfan@kth.se (K. Fan), jyfei@kth.se (Y. Ji), gkzhang@whut.edu.cn (G. Zhang), chenh3@sustech.edu.cn (H. Chen).

¹ These authors contributed equally.

² Leading author.

[21–23].

Unlike the Co-Pi and Co_xP catalysts which attract a lot of attention, the combination of cobalt cations with phosphite anions (Co²⁺-PO₃³⁻) to construct new types of Co-phosphite catalysts remain rarely been visited. Herein, by introducing the phosphite anions in the synthesis, we successfully discovered a microporous structured Co₁₁(HPO₃)₈(OH)₆ nanowires, which contains Ångström-scale hexagonal and triangular shaped pores. Close Co–Co metallic interaction has been also observed within the framework structure. The unique pore structure, metallic interaction and nanowire morphology physically guarantee the high conductivity and extended large surface area. Synergistically, the deprotonation of H⁺ on the framework phosphite anions group provides sufficient active sites and excellent activity when employing this material for OER. The present work not only bridges the gap between Co-Pi and Co_xP catalysts family with a lower overpotential, but also discloses the mechanism and active catalyst structure behind the improved catalytic efficiency based on the as-synthesized Co₁₁(HPO₃)₈(OH)₆ nanowires.

2. Results and discussion

Co₁₁(HPO₃)₈(OH)₆ nanowires were synthesized through hydrothermal process with an aqueous solution mixed with cobalt and phosphorous acid. The experimental details are described in the Supporting Information. As shown in Fig. 1a, the powder X-ray diffraction pattern (XRD) of the as-synthesized Co₁₁(HPO₃)₈(OH)₆ matches well with Co₁₁(HPO₃)₈(OH)₆ with JCPDS no.81–1064 and simulated PXRD based on ICSD No. of 72431, indicating the high purity and crystallinity of the obtained materials. The inductively coupled plasma optical emission spectroscopy (ICP-OES) data with Co/P atomic ratio of 1.362 is consistent with the theoretical value of 1.375 based on the chemical formula of Co₁₁(HPO₃)₈(OH)₆ (Table S2). Scanning electron microscopy (SEM) image (Fig. 1b) shows that the as-synthesized sample exhibits a sphere-like hierarchical structure, which is assembled from tremendous of nanowires. High angle annular dark-field (HAADF)

image (Fig. 1c) shows that the typical nanowire obtained from the crushed sphere with a width of ca. 25 nm and length around 10 μm. The associated energy-dispersive X-ray spectroscopy (EDS) mapping images (Fig. 1d–f) confirms the spatial distribution of the non-hydrogen elements in the Co₁₁(HPO₃)₈(OH)₆ nanowires. The crystal structure of Co₁₁(HPO₃)₈(OH)₆ is shown in Fig. 1g, the cobalt atoms are coordinated with six oxygen atoms to form a [CoO₆] octahedra, whereas two [CoO₆] octahedra are face-sharing with each other. These face-sharing [CoO₆] octahedra are further connected to other [CoO₆] octahedra by sharing the polyhedra edges. The Co–Co atomic distance in the two face-sharing octahedra is 2.757 Å, which is significantly shorter compared to other cobalt-oxo polyhedra involved compounds. This distance is even shorter than the critical distance in the Goodenough's formula ($R_c = 2.885 \text{ Å}$), indicating a metallic behaviour of these two Co atoms in Co₁₁(HPO₃)₈(OH)₆ [24]. The phosphor atoms are located within a [PO₃H] tetrahedral geometry surrounding with three oxygen atoms and one hydrogen atom, the extra hydrogen atoms from [PO₃H] tetrahedra in Co₁₁(HPO₃)₈(OH)₆ works as the hydrogen bond acceptor interacting with the water molecules within the microporous channels. Through the hydrogen bonding, this structure can be deprotonated in the aqueous environment, which may benefit the OER reaction. These polyhedra arrangements are similar to the Co-Pi catalysts reported by Nocera [18], as compared to the crystal structure of Co-Pi, both of them are phosphates or phosphite groups around the cobalt octahedra. Constructed by these [PO₃H] and [CoO₆] polyhedra, two different pore channels can be observed along the crystallographic *c* axis. The effective diameter of the channels is around 5 Å and 3 Å, respectively. Theoretically, the 5 Å diameter pores could provide great channels for the diffusion of small volume electrolyte ions, and gas molecules, thereby indicating a merit of this structure to be used for electrochemical catalytic reactions [25].

The electrochemical activity of oxygen evolution is characterized by a standard three-electrode system with Co₁₁(HPO₃)₈(OH)₆ loaded on the glassy carbon electrode (0.28 mg cm⁻²) in 1.0 M KOH. The working electrode is firstly activated by linear sweep voltammetry (LSV) until

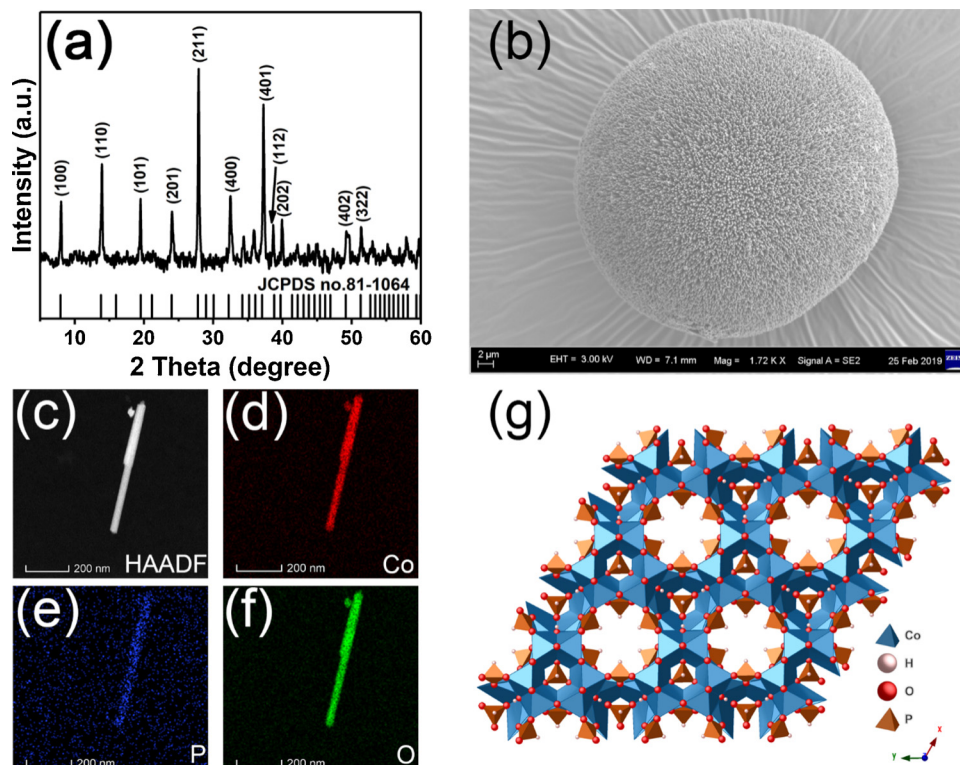


Fig. 1. (a) XRD pattern; (b) SEM; (c) HAADF and (d–f) EDS mapping images of the Co₁₁(HPO₃)₈(OH)₆ nanowires; (g) Crystal structure of Co₁₁(HPO₃)₈(OH)₆ view along the crystallographic *c* axis.

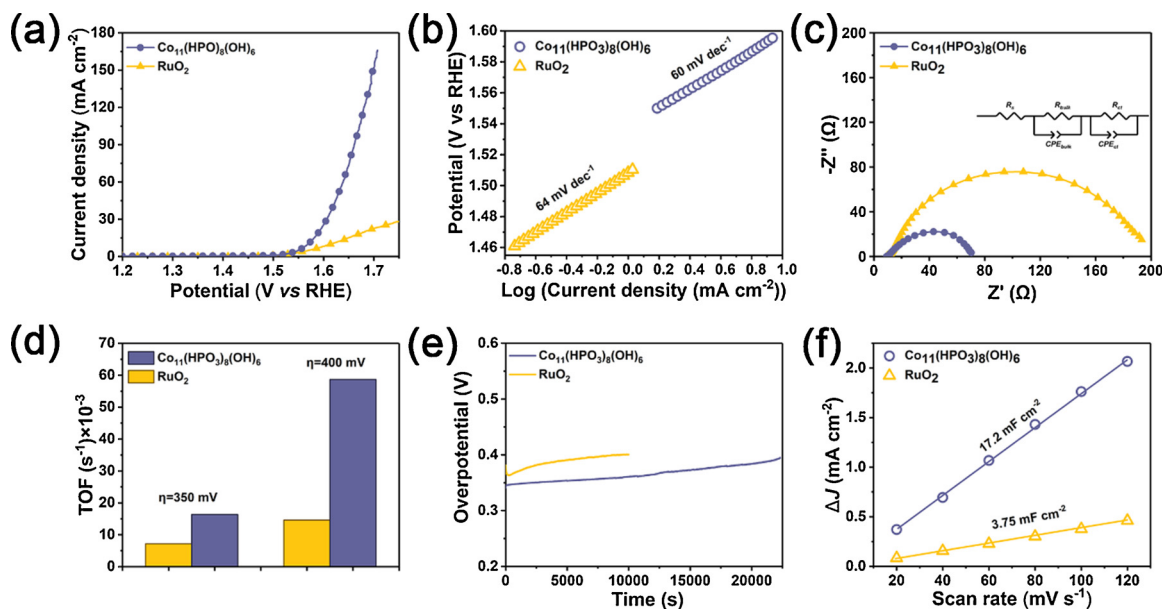


Fig. 2. (a) iR-compensated LSV curves, (b) Tafel slopes, (c) Nyquist plots (insert: equivalent circuit of catalysts), (d) TOFs (overpotential = 350 mV and 400 mV), (e) Chronopotentiometry curves, (f) C_{dl} of $\text{Co}_{11}(\text{HPO}_3)_8(\text{OH})_6$ and RuO_2 .

the stable curve is obtained. During this electrochemical activation process, the overpotential of at 10 mA cm^{-2} has been improved from the initial $\sim 370 \text{ mV}$ and eventually stabilized at $\sim 340 \text{ mV}$ (Fig. S4). This efficiency is better than the commercially purchased RuO_2 ($\sim 380 \text{ mV}$). Tafel slope, which has been used to extensively discuss the kinetic process of OER catalyst, has been given in Fig. 2b. Apparently, the Tafel slope of $\text{Co}_{11}(\text{HPO}_3)_8(\text{OH})_6$ is 60 mV dec^{-1} , which is slightly smaller than RuO_2 (64 mV dec^{-1}), showing a similar favorable dynamic reaction process. Such rapid OER process can further be illuminated by electrochemical impedance spectroscopy (EIS) test. As shown in the inset of Fig. 2c, in the equivalent circuit of OER catalyst, R_s represents the solution resistance, R_{ct} and R_{bulk} represent the interfacial and bulk charge trapping resistance, CPE_{ct} and CPE_{bulk} are described as constant phase elements of the interface and bulk, respectively. In the Nyquist plots, $\text{Co}_{11}(\text{HPO}_3)_8(\text{OH})_6$ shows smaller R_{ct} than RuO_2 which is in good coincidence with Bode plots (Fig. S1), indicating a good conductivity of the $\text{Co}_{11}(\text{HPO}_3)_8(\text{OH})_6$ electrode. Moreover, as the weight content of Co in the as-prepared sample has been tested to be 47% by ICP-AES. Hence, the turnover frequency (TOF) of $\text{Co}_{11}(\text{HPO}_3)_8(\text{OH})_6$ and RuO_2 has been calculated to be 0.016 and 0.007 s^{-1} at the overpotential of 350 mV , and 0.058 and 0.015 s^{-1} at the overpotential of 400 mV respectively (Fig. 2d), assuming all the metal sites in the catalyst are active. These observation results prove a better electrocatalytic activity of the $\text{Co}_{11}(\text{HPO}_3)_8(\text{OH})_6$ catalyst. To test the stability of the catalyst, the chronopotentiometry curves are recorded in Fig. 2e with a current density of 10 mA cm^{-2} . $\text{Co}_{11}(\text{HPO}_3)_8(\text{OH})_6$ requires a relatively stable overpotential of $\sim 350 \text{ mV}$, which increases slightly to $\sim 380 \text{ mV}$ after $\sim 6.5 \text{ h}$ measurement, while RuO_2 needs a larger overpotential of $\sim 400 \text{ mV}$ with similar stability. These results indicate that $\text{Co}_{11}(\text{HPO}_3)_8(\text{OH})_6$ has higher activity but similar long-term stability comparable with RuO_2 .

To further understand the catalytic performance, electrochemically active surface area (ECSA) is positively correlated with electrochemical double-layer capacitance (C_{dl}), so C_{dl} is calculated for the electrocatalyst based on the cyclic voltammetry (CV), which is measured under different scan rates in non-faradaic potential range (Fig. S2) [5]. According to Fig. 2f, the C_{dl} of $\text{Co}_{11}(\text{HPO}_3)_8(\text{OH})_6$ is 17.2 mF cm^{-2} in term of capacitance, which is more than four times of that of RuO_2 (3.75 mF cm^{-2}), partially being ascribed to the refinement of nanowires which can provide great quantity of potential active sites. As

illustrated above, the combined electrochemical analytical measurements give adequate proof of promising application of $\text{Co}_{11}(\text{HPO}_3)_8(\text{OH})_6$ for OER in an alkaline environment.

To check the morphology and nanowire structure stability, SEM image has been taken for the catalyst after OER reaction. As shown in Fig. S3c, the catalyst remains a sphere-like structure assembled with nanowires. Some amorphous materials stick on it which should be contributed by the conductive binder Nafion polymer. To further check the crystallographic structure stability of the catalyst after OER, *ex-situ* grazing incidence wide-angle X-ray scattering (GIWAXS) was collected at Stanford Synchrotron Radiation Lightsources (SSRL) at the beamline 11-3 with the as-made fluorine doped tin oxide (FTO) electrode after long-term OER electrolysis. The corresponding 2D powder X-ray diffraction (XRD) pattern has been extracted and illustrated in Fig. 3b. Based on the GIWAXS data, the diffraction peak position matches well with the simulated PXRD pattern of $\text{Co}_{11}(\text{HPO}_3)_8(\text{OH})_6$ and SnO_2 (JCPDS no. 77-0415), indicating that from crystallography point of view, there is no crystallographic phase transition can be observed with the thickness sensitive GIWAXS technique, as typically GIWAX technique is sensitive to the phase determination in a sample down to a few nanometers thickness. Moreover, individual nano-sized crystalline phase sensitive rotation electron diffraction (RED) techniques [26–29], with great advantage to obtain unit cell and determine crystal structure for nanosized crystals, was used to study the individual particles crystal structure for the catalyst after OER. More than five different RED data have been collected for different nanocrystals scratched from the electrode after OER. All the collected RED data show good diffraction quality similar to the data presented in Fig. 3c–f. A unit cell of $a = 13.094 \text{ \AA}$, $b = 12.966 \text{ \AA}$, $c = 5.185 \text{ \AA}$, $\alpha = 90.54^\circ$, $\beta = 89.49^\circ$, $\gamma = 118.69^\circ$ can be obtained from the above data. Considering of the error of the RED technique [30], the unit cell parameters of the post-catalyst are in well agreement with the initial ones obtained from X-ray diffraction, where $a = 12.824 \text{ \AA}$, $b = 12.824 \text{ \AA}$, $c = 4.973 \text{ \AA}$, $\alpha = 90^\circ$, $\beta = 90^\circ$, $\gamma = 120^\circ$. This observation indicates that there is no crystallography phase change during the OER. Based on the SEM, GIWAX and RED study, we could conclude here that after OER reaction, the nanowires maintain their crystallography phase from their bulk to their outer surface down to a few nanometers thickness. The structure difference of the nanowires before and after OER is non-detectable with both imaging and diffraction techniques.

To further elucidate the structure changes which responsible for the

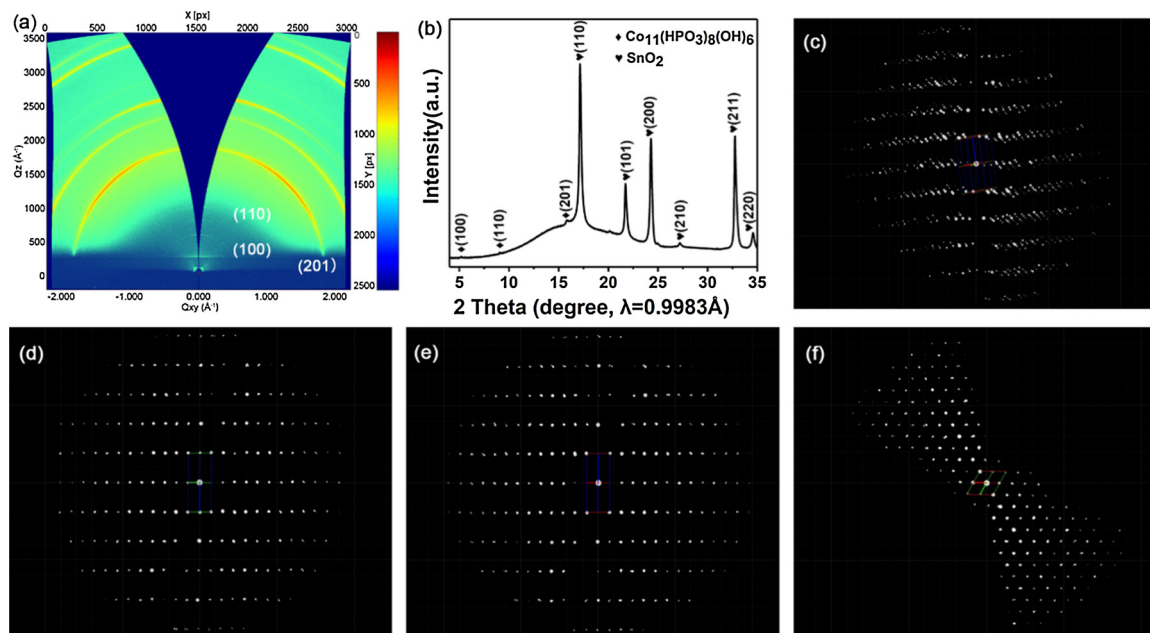


Fig. 3. (a) 2D GIWAX pattern of the electrode after OER; (b) 2D XRD pattern derived from GIWAX pattern; (c) The overview of the reconstructed 3D reciprocal lattice of the RED data; The 3D reciprocal lattice view along the (d) a^* axis, (e) b^* axis, (f) c^* axis. (For interpretation of the references to colour in this figure legend, the reader is referred to the web version of this article).

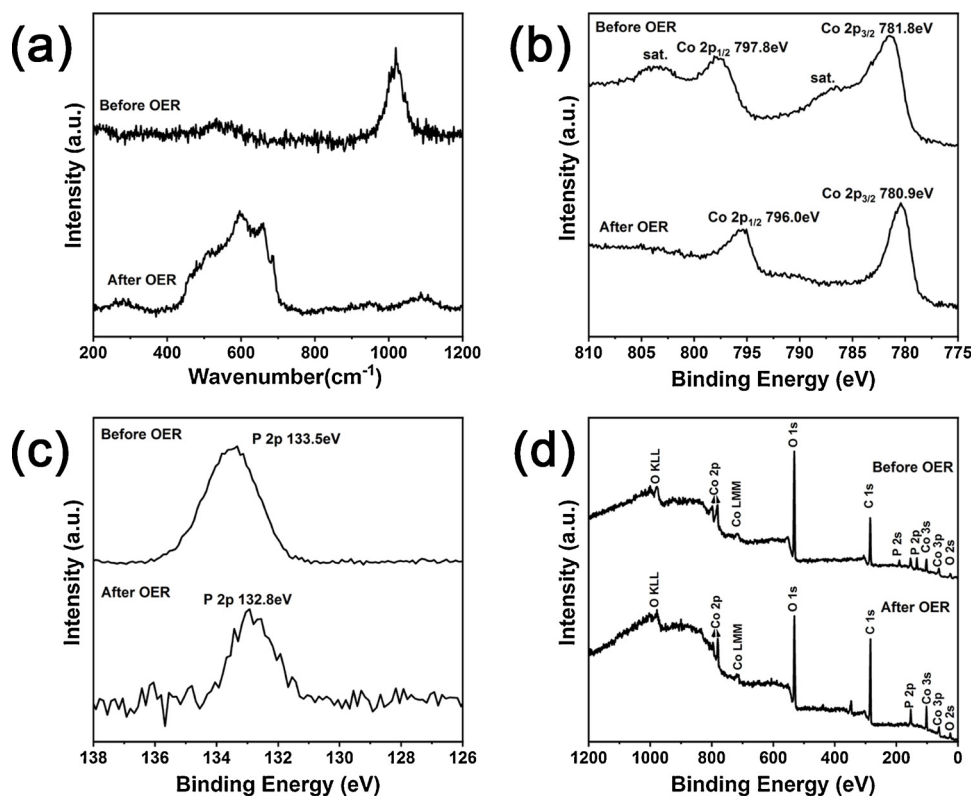


Fig. 4. (a) Raman spectra, high-resolution XPS spectra for (b) Co 2p, (c) P 2p, and Overall XPS spectra of the pre-catalytic sample and post-catalytic sample.

improving of OER activity during the activation process, surface sensitive techniques within sub-nanometer range sensitivity, such as Raman spectroscopy and X-ray photoelectron spectroscopy (XPS), have been employed. Before OER, a Raman band (Fig. 4a) at around 1018 cm^{-1} can be assigned to the PO $^-$ bending mode, which is the characteristic band of phosphite anions (PO_3^{3-}) [31,32]; Another band at ca. 536 cm^{-1} can be ascribed to oxygen vibration similar to Co–O

stretching modes in Co_3O_4 [33–36]. After electrocatalysis for 24 h, the Raman bands has a broad peak at 600 cm^{-1} . Moreover, X-ray photon electron spectroscopy (XPS) with the surface sensitivity of sub-nanometers has been employed to study the surface chemistry and electronic structures. As shown in Fig. 4b, before the OER, the cobalt $2p_{1/2}$ and $2p_{3/2}$ XPS peaks are located at 781.8 eV and 797.8 eV, respectively, with two extra shake-up satellite peaks observed [37–39]. The Co with

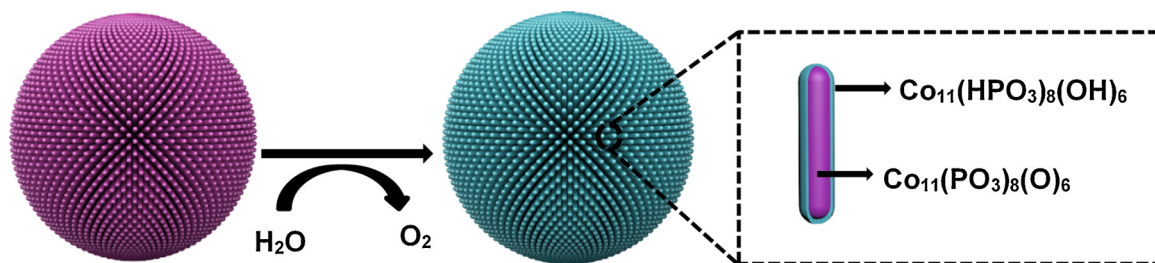


Fig. 5. Schematic illustration of the in situ reassembly of $\text{Co}_{11}(\text{HPO}_3)_8(\text{OH})_6$ nanowires surface.

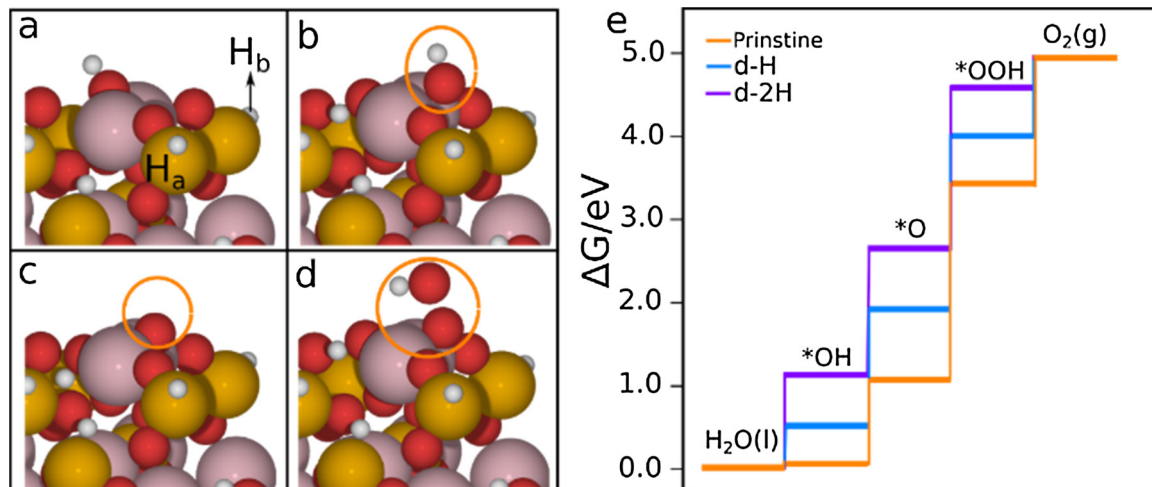


Fig. 6. (a) The bare substrate; (b)-(d), Optimized adsorption geometries of the intermediates $^*\text{OH}$, $^*\text{O}$ and $^*\text{OOH}$; (e), The free energy landscape on the pristine surface (orange), with H_a removed (blue), and with both H_a and H_b removed (purple). (For interpretation of the references to colour in this figure legend, the reader is referred to the web version of this article).

the Co(II) oxidation state has been confirmed, which is well consistent with the valence state deduced from the chemical formula of $\text{Co}_{11}(\text{HPO}_3)_8(\text{OH})_6$ [40]. After the OER, the satellite peaks are greatly reduced, indicating that most of the cobalt cations has been converted to a higher oxidation state, which is consistent with the observations in the reported $\text{Co}(\text{PO}_3)_2$ materials [36,41]. The peak centered at 133.5 eV and 132.8 eV in Fig. 4c can be specified as P 2p, indicating the presence of electron deficient phosphorus species near the surface [42,43]. The slight shift can be ascribed to oxidation of surface phosphorus atom in the nanowires [44].

Based on the comprehensive study by employing the different thickness sensitive techniques for surface and nano-sized bulk structure probing, it could be concluded that during the OER, the as-synthesized $\text{Co}_{11}(\text{HPO}_3)_8(\text{OH})_6$ nanowires remain their crystallographic crystal structure. While on the catalyst surface, extending within sub-nanometer thickness, the catalyst undergoes surface rearrangement, most probably forming a thin layer of high oxidation cobalt phosphite on the surface of $\text{Co}_{11}(\text{HPO}_3)_8(\text{OH})_6$. As the surface layer is too thin, it might be just a crystalline layer with structure difference undetectable with high sensitive diffraction or imaging techniques, when it is coexisting with the as-synthesized $\text{Co}_{11}(\text{HPO}_3)_8(\text{OH})_6$ nanowires. Considered in the $\text{Co}_{11}(\text{HPO}_3)_8(\text{OH})_6$ crystal structure, there are plenty of proton binding on the phosphite groups. Under the alkaline and electrochemical condition used in OER, the proton on the phosphite anions might be deprotonated and reacted with the hydroxide anions, thus excites the cobalt with higher valence state. The catalytic performance improvement, as indicated by the LSV curves at the first 5 circles (Fig. S4), might be benefited from the surface layer of protonated $\text{Co}_{11}(\text{PO}_3)_8(\text{O})_6$ with less proton but higher valence state of cobalt and phosphorous atoms. Eventually, it is forming a stable lower overpotential of core-shell structural $\text{Co}_{11}(\text{HPO}_3)_8(\text{OH})_6/\text{Co}_{11}(\text{PO}_3)_8(\text{O})_6$

nanowire active catalyst in alkaline environment. Moreover, the metallic behavior resulting from the shorter Co-Co interatomic distance within the crystal structure could also facilitate the electron transportation from the nanowire to the surface layer of the oxidized species (Fig. 5). The observed catalytic activity might come from the $\text{Co}_{11}(\text{HPO}_3)_8(\text{OH})_6$ nanowire encapsulated by the deprotonated $\text{Co}_{11}(\text{PO}_3)_8(\text{O})_6$ with the synergistic effect of the oxidized out-shell species and support material. Meanwhile, due to the elevated valence of phosphorus, the exposed sites of the deprotonated phosphite group actively attract the hydroxyl groups from the water and catalyze the oxygen evolution. That is why a superior catalytic efficiency has been observed. One point should be noted here is that, although the difference of $\text{Co}_{11}(\text{HPO}_3)_8(\text{OH})_6$ and $\text{Co}_{11}(\text{PO}_3)_8(\text{O})_6$ could be well distinguished from crystal structure point of view, based on the spatial distribution of hydrogen in the nanowires. While due to the lacking of efficient characterization technique for probing the spatial distribution of hydrogen atoms, the boundary of $\text{Co}_{11}(\text{HPO}_3)_8(\text{OH})_6$ and $\text{Co}_{11}(\text{PO}_3)_8(\text{O})_6$ is not clear yet.

To further illustrate the dynamical catalytical structure process, density function theory (DFT) has been employed to illustrate the mechanism behind the OER process. The optimized structure of the intermediates and the free energy surfaces are shown in Fig. 6. The preferred exposure surface of the crystallographic (100) plane has been chosen for DFT modelling as $\text{Co}_{11}(\text{HPO}_3)_8(\text{OH})_6$ crystallized in hexagonal space group with nanowire structure. On the pristine $\text{Co}_{11}(\text{HPO}_3)_8(\text{OH})_6$ -(100) surface, the overpotential is calculated to be 1.13 eV. When a H atom (H_a in figure 5a) on the neighbouring P is removed, the overpotential is lowered to 0.80 eV; when both H_a and H_b are removed, the overpotential is further lowered to 0.70 eV. These results suggest that the performance of $\text{Co}_{11}(\text{HPO}_3)_8(\text{OH})_6$ can be improved when more H atoms were removed on the original catalyst

structure, which is in agreement with the experiment that deprotonation do contribute to the catalytic activity improvement and a core-shell structured $\text{Co}_{11}(\text{HPO}_3)_8(\text{OH})_6/\text{Co}_{11}(\text{PO}_3)_8\text{O}_6$ might be formed and work as the active OER catalyst.

3. Conclusions

In summary, we report the first cobalt phosphite nanowire with core-shell structure of $\text{Co}_{11}(\text{HPO}_3)_8(\text{OH})_6/\text{Co}_{11}(\text{PO}_3)_8\text{O}_6$ exhibits high OER performance in an alkaline environment. GIWAX and RED reveal the internal crystal structure without observable crystallographic phase evolution during the catalytic cycles, while Raman, XPS and DFT indicate that surface deprotonation and oxidation are occurring in the $\text{Co}_{11}(\text{HPO}_3)_8(\text{OH})_6$ electrocatalyst during electrocatalysis. The rich active sites, good electron conductivity, surface deprotonation and oxidation which can lower the over potential, are the main factors responsible for the enhancement of OER performance in the $\text{Co}_{11}(\text{HPO}_3)_8(\text{OH})_6$ OER nanowire. The present work paves the way for exploring novel high efficiency water splitting catalysts based on the new combination of Co- PO_3 rather than Co^{2+} - PO_4^{3-} and Co^{2+} - P^{3-} .

Declaration of Competing Interest

The authors declare that they have no known competing financial interests or personal relationships that could have appeared to influence the work reported in this paper.

Acknowledgments

This work was financially supported by the National Natural Science Foundation of China (21777045). H.C acknowledges the Start-up funding provided by SUSTech. The research used resource at the Stanford Synchrotron Radiation Light Source at SLAC National Accelerator Laboratory supported by the U.S. Department of Energy, Office of Science, Basic Energy Sciences under contract no. DE-AC02-76SF00515.

Appendix A. Supplementary data

Supplementary material related to this article can be found, in the online version, at doi:<https://doi.org/10.1016/j.apcatb.2019.118091>.

References

- [1] J. Wang, W. Cui, Q. Liu, Z. Xing, A.M. Asiri, X. Sun, Recent progress in cobalt-based heterogeneous catalysts for electrochemical water splitting, *Adv. Mater.* 28 (2016) 215–230, <https://doi.org/10.1002/adma.201502696>.
- [2] S. Zhao, M. Li, M. Han, D. Xu, J. Yang, Y. Lin, N.-E. Shi, Y. Lu, R. Yang, B. Liu, Z. Dai, J. Bao, Defect-rich Ni₃FeN nanocrystals anchored on N-doped graphene for enhanced electrocatalytic oxygen evolution, *Adv. Funct. Mater.* 28 (2018) 1706018, <https://doi.org/10.1002/adfm.201706018>.
- [3] X. Zhao, X. Li, Y. Yan, Y. Xing, S. Lu, L. Zhao, S. Zhou, Z. Peng, J. Zeng, Electrical and structural engineering of cobalt selenide nanosheets by Mn modulation for efficient oxygen evolution, *Appl. Catal. B Environ.* 236 (2018) 569–575, <https://doi.org/10.1016/j.apcatb.2018.05.054>.
- [4] P.T. Babar, A.C. Lokhande, B.S. Pawar, M.G. Gang, E. Jo, C. Go, M.P. Suryawanshi, S.M. Pawar, J.H. Kim, Electrocatalytic performance evaluation of cobalt hydroxide and cobalt oxide thin films for oxygen evolution reaction, *Appl. Surf. Sci.* 427 (2018) 253–259, <https://doi.org/10.1016/j.apsusc.2017.07.142>.
- [5] H. Zou, B. He, P. Kuang, J. Yu, K. Fan, Metal-organic framework-derived nickel-cobalt sulfide on ultrathin mxene nanosheets for electrocatalytic oxygen evolution, *ACS Appl. Mater. Interfaces* 10 (2018) 22311–22319, <https://doi.org/10.1021/acsami.8b06272>.
- [6] Q. Liu, L. Xie, Z. Liu, G. Du, A.M. Asiri, X. Sun, A Zn-doped Ni₃S₂ nanosheet array as a high-performance electrochemical water oxidation catalyst in alkaline solution, *Chem. Commun.* 53 (2017) 12446–12449, <https://doi.org/10.1039/C7CC06668F>.
- [7] Q. Liu, L. Xie, F. Qu, Z. Liu, G. Du, A.M. Asiri, X. Sun, A porous Ni₃N nanosheet array as a high-performance non-noble-metal catalyst for urea-assisted electrochemical hydrogen production, *Inorg. Chem. Front.* 4 (2017) 1120–1124, <https://doi.org/10.1039/C7QI00185A>.
- [8] Y.-Q. Zhang, M. Li, B. Hua, Y. Wang, Y.-F. Sun, J.-L. Luo, A strongly cooperative spinel nanohybrid as an efficient bifunctional oxygen electrocatalyst for oxygen reduction reaction and oxygen evolution reaction, *Appl. Catal. B Environ.* 236 (2018) 413–419, <https://doi.org/10.1016/j.apcatb.2018.05.047>.
- [9] L. Xie, F. Qu, Z. Liu, X. Ren, S. Hao, R. Ge, G. Du, A.M. Asiri, X. Sun, L. Chen, In situ formation of a 3D core/shell structured Ni₃N@Ni-Bi nanosheet array: an efficient non-noble-metal bifunctional electrocatalyst toward full water splitting under near-neutral conditions, *J. Mater. Chem. A* 5 (2017) 7806–7810, <https://doi.org/10.1039/C7TA02333B>.
- [10] J. Yang, D. Guo, S. Zhao, Y. Lin, R. Yang, D. Xu, N. Shi, X. Zhang, L. Lu, Y.-Q. Lan, J. Bao, M. Han, Cobalt phosphides nanocrystals encapsulated by P-doped carbon and married with P-doped graphene for overall water splitting, *Small* 15 (2019) 1804546, <https://doi.org/10.1002/sml.201804546>.
- [11] P. Kuang, M. He, H. Zou, J. Yu, K. Fan, OD/3D MoS₂-NiS₂/N-doped graphene foam composite for efficient overall water splitting, *Appl. Catal. B Environ.* 254 (2019) 15–25, <https://doi.org/10.1016/j.apcatb.2019.04.072>.
- [12] P. Li, R. Zhao, H. Chen, H. Wang, P. Wei, H. Huang, Q. Liu, T. Li, X. Shi, Y. Zhang, M. Liu, X. Sun, Recent advances in the development of water oxidation electrocatalysts at mild pH, *Small* 15 (2019) 1805103, <https://doi.org/10.1002/sml.201805103>.
- [13] P. Chen, K. Xu, Z. Fang, Y. Tong, J. Wu, X. Lu, X. Peng, H. Ding, C. Wu, Y. Xie, Metallic Co 4 N porous nanowire arrays activated by surface oxidation as electrocatalysts for the oxygen evolution reaction, *Angew. Chem. Int. Ed.* 54 (2015) 14710–14714, <https://doi.org/10.1002/anie.201506480>.
- [14] M. Kim, S. Kim, D. Song, S. Oh, K.J. Chang, E. Cho, Promotion of electrochemical oxygen evolution reaction by chemical coupling of cobalt to molybdenum carbide, *Appl. Catal. B Environ.* 227 (2018) 340–348, <https://doi.org/10.1016/j.apcatb.2018.01.051>.
- [15] Y. Chang, N.E. Shi, S. Zhao, D. Xu, C. Liu, Y.J. Tang, Z. Dai, Y.Q. Lan, M. Han, J. Bao, Coraloid Co₂P₂O₇ nanocrystals encapsulated by thin carbon shells for enhanced electrochemical water oxidation, *ACS Appl. Mater. Interfaces* 8 (2016) 22534–22544, <https://doi.org/10.1021/acsami.6b07209>.
- [16] N. Jiang, B. You, M. Sheng, Y. Sun, Electrodeposited cobalt-phosphorous-derived films as competent bifunctional catalysts for overall water splitting, *Angew. Chem. Int. Ed.* 54 (2015) 6251–6254, <https://doi.org/10.1002/anie.201501616>.
- [17] H. Li, P. Wen, Q. Li, C. Dun, J. Xing, C. Lu, S. Adhikari, L. Jiang, D.L. Carroll, S.M. Geyer, Earth-abundant iron diboride (FeB₂) nanoparticles as highly active bifunctional electrocatalysts for overall water splitting, *Adv. Energy Mater.* 7 (2017) 1700513, <https://doi.org/10.1002/aenm.201700513>.
- [18] M.W. Kanan, D.G. Nocera, In situ formation of an oxygen-evolving catalyst in neutral water containing phosphate and Co²⁺, *Science* 321 (2008) 1072–1075, <https://doi.org/10.1126/science.1162018>.
- [19] S. Cobo, J. Heidkamp, P.-A. Jacques, J. Fize, V. Fourmond, L. Guetaz, B. Jousseme, V. Ivanova, H. Dau, S. Palacin, M. Fontecave, V. Artero, A Janus cobalt-based catalytic material for electro-splitting of water, *Nat. Mater.* 11 (2012) 802–807, <https://doi.org/10.1038/nmat3385>.
- [20] C.-Z. Yuan, Y.-F. Jiang, Z. Wang, X. Xie, Z.-K. Yang, A. Bin Yousaf, A.-W. Xu, Cobalt phosphate nanoparticles decorated with nitrogen-doped carbon layers as highly active and stable electrocatalysts for the oxygen evolution reaction, *J. Mater. Chem. A* 4 (2016) 8155–8160, <https://doi.org/10.1039/C6TA01929C>.
- [21] R. Gond, D.K. Singh, M. Eswaramoorthy, P. Barpanda, Sodium cobalt metaphosphate as an efficient oxygen evolution reaction catalyst in alkaline solution, *Angew. Chem. Int. Ed.* 58 (2019) 8330–8335, <https://doi.org/10.1002/anie.201901813>.
- [22] T. Di, B. Zhu, J. Zhang, B. Cheng, J. Yu, Enhanced photocatalytic H₂ production on CdS nanorod using cobalt-phosphate as oxidation cocatalyst, *Appl. Surf. Sci.* 389 (2016) 775–782, <https://doi.org/10.1016/j.apsusc.2016.08.002>.
- [23] Y. Pan, K. Sun, Y. Lin, X. Cao, Y. Cheng, S. Liu, L. Zeng, W.-C. Cheong, D. Zhao, K. Wu, Z. Liu, Y. Liu, D. Wang, Q. Peng, C. Chen, Y. Li, Electronic structure and d-band center control engineering over M-doped CoP (M = Ni, Mn, Fe) hollow polyhedron frames for boosting hydrogen production, *Nano Energy* 56 (2019) 411–419, <https://doi.org/10.1016/j.nanoen.2018.11.034>.
- [24] M. Butel, Cobalt oxyhydroxides obtained by “chimie douce” reactions: structure and electronic conductivity properties, *Solid State Ion.* 122 (1999) 271–284, [https://doi.org/10.1016/S0167-2738\(99\)00076-4](https://doi.org/10.1016/S0167-2738(99)00076-4).
- [25] D.H. Lee, M. Kang, S.-M. Paek, H. Jung, Study on the Electrochemical Property of Microporous Cobalt Phosphite [Co₁₁(HPO₃)₈(OH)₆], *Bull. Korean Chem. Soc.* 37 (2016) 192–199, <https://doi.org/10.1002/bkcs.10652>.
- [26] J. Lin, M. Lai, L. Dou, C.S. Kley, H. Chen, F. Peng, J. Sun, D. Lu, S.A. Hawks, C. Xie, F. Cui, A.P. Alivisatos, D.T. Limmer, P. Yang, Thermochromic halide perovskite solar cells, *Nat. Mater.* 17 (2018) 261–267, <https://doi.org/10.1038/s41563-017-0006-0>.
- [27] W. Hua, H. Chen, Z.-B. Yu, X. Zou, J. Lin, J. Sun, A germanosilicate structure with 11 × 11 × 12-Ring channels solved by electron crystallography, *Angew. Chem. Int. Ed.* 53 (2014) 5868–5871, <https://doi.org/10.1002/anie.201309766>.
- [28] H. Chen, J. Ju, Q. Meng, J. Su, C. Lin, Z. Zhou, G. Li, W. Wang, W. Gao, C. Zeng, C. Tang, J. Lin, T. Yang, J. Sun, PKU-3: an HCl-Inclusive aluminoborate for Strecker reaction solved by combining RED and PXRD, *J. Am. Chem. Soc.* 137 (2015) 7047–7050, <https://doi.org/10.1021/jacs.5b03685>.
- [29] T. Willhammar, J. Sun, W. Wan, P. Oleynikov, D. Zhang, X. Zou, M. Moliner, J. Gonzalez, C. Martínez, F. Rey, A. Corma, Structure and catalytic properties of the most complex intergrown zeolite ITQ-39 determined by electron crystallography, *Nat. Chem.* 4 (2012) 188–194, <https://doi.org/10.1038/nchem.1253>.
- [30] W. Wan, J. Sun, J. Su, S. Hovmöller, X. Zou, Three-dimensional rotation electron diffraction: software RED for automated data collection and data processing, *J. Appl. Crystallogr.* 46 (2013) 1863–1873, <https://doi.org/10.1107/S0021889813027714>.
- [31] M.I. Arriortua, T. Rojo, J.L. Mesa, S. Fernández, L. Lezama, J.L. Pizarro,

- Hydrothermal synthesis of a new layered inorganic–organic hybrid cobalt(II) phosphite: $(\text{C}_2\text{H}_{10}\text{N}_2)[\text{Co}_3(\text{HPO}_3)_4]$, *Int. J. Inorg. Mater.* 3 (2002) 331–336, [https://doi.org/10.1016/s1466-6049\(01\)00031-9](https://doi.org/10.1016/s1466-6049(01)00031-9).
- [32] R. Gond, R.P. Rao, V. Pralong, O.I. Lebedev, S. Adams, P. Barpanda, Cubic sodium cobalt metaphosphate $[\text{NaCo}(\text{PO}_3)_3]$ as a cathode material for sodium ion batteries, *Inorg. Chem.* 57 (2018) 6324–6332, <https://doi.org/10.1021/acs.inorgchem.8b00291>.
- [33] X. Wang, L. Song, H. Yang, W. Xing, H. Lu, Y. Hu, Cobalt oxide/graphene composite for highly efficient CO oxidation and its application in reducing the fire hazards of aliphatic polyesters, *J. Mater. Chem.* 22 (2012) 3426, <https://doi.org/10.1039/c2jm15637g>.
- [34] K.P. Reddy, R. Jain, M.K. Ghosalya, C.S. Gopinath, Metallic cobalt to spinel Co_3O_4 -electronic structure evolution by near-ambient pressure photoelectron spectroscopy, *J. Phys. Chem. C* 121 (2017) 21472–21481, <https://doi.org/10.1021/acs.jpcc.7b06661>.
- [35] B.S. Yeo, A.T. Bell, Enhanced activity of gold-supported cobalt oxide for the electrochemical evolution of oxygen, *J. Am. Chem. Soc.* 133 (2011) 5587–5593, <https://doi.org/10.1021/ja200559j>.
- [36] H.S. Ahn, T.D. Tilley, Electrocatalytic water oxidation at neutral pH by a nanostructured $\text{Co}(\text{PO}_3)_2$ anode, *Adv. Funct. Mater.* 23 (2013) 227–233, <https://doi.org/10.1002/adfm.201200920>.
- [37] B. Li, Y. Shi, K. Huang, M. Zhao, J. Qiu, H. Xue, H. Pang, Cobalt-doped nickel phosphite for high performance of electrochemical energy storage, *Small* 14 (2018) 1703811, <https://doi.org/10.1002/sml.201703811>.
- [38] C. Qi, L. Zhang, G. Xu, Z. Sun, A. Zhao, D. Jia, $\text{Co}@\text{Co}_3\text{O}_4$ nanoparticle embedded nitrogen-doped carbon architectures as efficient bicatalysts for oxygen reduction and evolution reactions, *Appl. Surf. Sci.* 427 (2018) 319–327, <https://doi.org/10.1016/j.apsusc.2017.08.209>.
- [39] W.-K. Gao, J.-F. Qin, K. Wang, K.-L. Yan, Z.-Z. Liu, J.-H. Lin, Y.-M. Chai, C.-G. Liu, B. Dong, Facile synthesis of Fe-doped Co_9S_8 nano-microspheres grown on nickel foam for efficient oxygen evolution reaction, *Appl. Surf. Sci.* 454 (2018) 46–53, <https://doi.org/10.1016/j.apsusc.2018.05.099>.
- [40] T.J. Chuang, C.R. Brundle, D.W. Rice, Interpretation of the x-ray photoemission spectra of cobalt oxides and cobalt oxide surfaces, *Surf. Sci.* 59 (1976) 413–429.
- [41] S.W. Ho, M. Houalla, D.M. Hercules, Effect of particle size on carbon monoxide hydrogenation activity of silica supported cobalt catalysts, *J. Phys. Chem.* 94 (1990) 6396–6399, <https://doi.org/10.1021/j100379a045>.
- [42] M. Weil, M. Puchberger, J.S.A. Der G  nne, J. Weber, Synthesis, crystal structure, and characterization (vibrational and solid-state ^{31}P MAS NMR spectroscopy) of the high-temperature modification of calcium catena-polyphosphate(V), *Chem. Mater.* 19 (2007) 5067–5073, <https://doi.org/10.1021/cm071239i>.
- [43] A.P. Grosvenor, S.D. Wik, R.G. Cavell, A. Mar, Examination of the bonding in binary transition-metal monophosphides MP (M = Cr, Mn, Fe, Co) by X-ray photoelectron spectroscopy, *Inorg. Chem.* 44 (2005) 8988–8998, <https://doi.org/10.1021/ic051004d>.
- [44] J.F. Moulder, W.F. Stickle, P.E. Sobol, K.D. Bomben, J. Chastain (Ed.), *Handbook of X-Ray Photoelectron Spectroscopy*, Perkin-Elmer Corp., Eden Prairie, MN, 1992.